INSTITUTE OF PHYSICS PUBLISHING JOURNAL OF OPTICS A: PURE AND APPLIED OPTICS

J. Opt. A: Pure Appl. Opt. **4** (2002) S369–S375 PII: S1464-4258(02)37349-5

New interferometric technique for piston measurement in segmented mirrors

A Pintó, F Laguarta, R Artigas and C Cadevall

Center for Sensors, Instruments and Systems Development (CD6), Technical University of Catalonia (UPC), Rambla Sant Nebridi, 10 E-08222 Terrassa, Spain

E-mail: pinto@oo.upc.es, laguarta@oo.upc.es, rartigas@oo.upc.es and cristina.cadevall@upc.es

Received 17 May 2002, in final form 2 August 2002
Published 4 November 2002
Online at stacks.iop.org/JOptA/4/S369

Abstract
Present trends in the design of ground-based telescopes point towards the use of segmented primary mirrors. A major problem in this type of mirror is the achievement of proper segment positioning, as they have to be aligned with an accuracy of the order of a fraction of a wavelength for near-diffraction-limit telescope performance in the infrared. In this paper we present a new interferometric technique applied to the measurement of segment vertical misalignment (piston error) in segmented mirrors. The instrument is based on a high-aperture Michelson interferometer using a broadband light spectrum. The main innovation introduced in this instrument is the use of a novel optical fibre illumination technique that allows the system to measure piston error during the daytime with an uncertainty of 5 nm in a 30 μm range. A detailed description of the light spectrum, expected interferograms and piston extraction algorithms is presented here.

Keywords: Metrology, data analysis, interferometer, optical testing technique, ground-based optical telescope

(Some figures in this article are in colour only in the electronic version)

1. Introduction

Since their invention in the 16th century, telescopes have evolved from Galileo's original to the 10 m twin Keck telescopes, with constant increases in primary mirror diameter. By using larger primary mirrors, both the light gathering power and angular resolution of a telescope are increased. Historically, a larger telescope was obtained by simply scaling up the existing technology, the mirror being made of a single piece of glass (the *monolithic approach*). However, a limit was reached when mirrors wider than 8 m were needed, as scaling up the monolithic approach was not practical nor affordable due basically to the large mass required and the difficulties of the figuring process. At the beginning of the 1980s the *segmented approach* in designing and building large telescope primary mirrors was developed. Since then, the use of segmented mirrors (see figure 1), where a number of smaller mirrors called segments, arranged like a mosaic, work together to provide an image quality and aperture equivalent to that of a large monolithic mirror, has become crucial and will continue to be so in the development of future generations of ground-based telescopes.

However, some new problems arise with the segmented approach. One of these is proper relative segment positioning. Some other factors, such as individual segment figure, have a strong effect on the achievement of diffraction-limited images in the infrared, but proper segment positioning is a major factor in this regard. This new approach in designing and building large ground-based telescopes requires an external calibration system (called a 'phasing system') that measures relative segment misalignment. The misalignment is then corrected using a set of actuators located below each segment. Once this procedure (known as the 'phasing procedure') has been carried out the mirror is said to be 'phased' and it is ready for scientific observation. The segment positions are held stable against gravitational and thermal 'perturbations' using

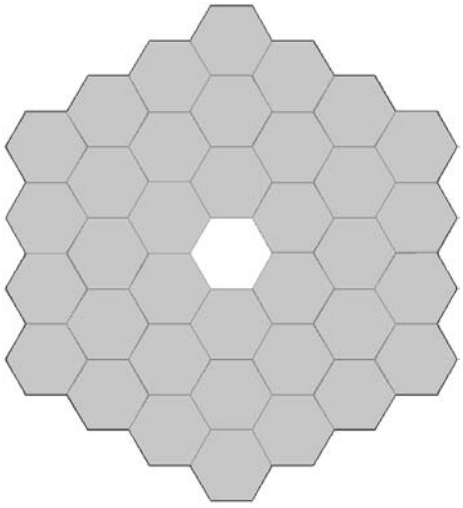

Figure 1. 36-element segmented mirror.

an active position control system. However, the active control system suffers from drift and periodic 'phasing' is required.

There are two types of out-of-plane segment misalignments: relative rotations (called tip and tilt, see figure 2(*a*)) and vertical displacement (called piston, see figure 2(*b*)), as the segments cannot move in the other degrees of freedom due to the segment support system. Relative segment angular misalignments produce individual images of the distant object in the image plane. By removing tip and tilt all these images are superposed. To achieve a diffraction-limited performance in the infrared as well as proper operation of adaptive optics (AO) instruments, these images must be superposed coherently; this requires the steps between segments to be removed down to a small fraction of a wavelength (Chanan *et al* 1998).

Currently, only a few segmented mirror telescopes are operational (the W M Keck telescopes and Hobby Eberly Telescope (HET)) but others are being built or designed (Gran Telescopio Canarias (GTC), Southern African Large Telescope (SALT), Telescopio Infrarrojo Mexicano (TIM), California Extremely Large Telescope (CELT), etc).

Recently, the international astronomical community has shown a growing interest in the development of daytime phasing systems, as most of the techniques proposed for use in a 'phasing system', as well as the one used regularly to 'phase' the Keck telescopes, have the drawback that they are starlight-based techniques, with the consequent loss of astronomical observation time. In an earlier paper (Pizarro *et al* 2002) we presented the design of an interferometer named UPC-ZEBRA, designed specifically to measure relative segment misalignment during the daytime. This instrument has been developed according to the basic design guidelines for a phasing system that can be found in the GTC conceptual design (Grantecan 1997). Here we present a detailed theoretical description of both the interferograms obtained with the instrument and the processing algorithms used to extract the segment misalignment from them.

In section 2, a brief description of the instrument developed is included for completeness. In section 3, a theoretical description of the novel illumination spectrum used is presented. In section 4, a simulation of the expected interferograms using this illumination spectrum is done. The following section presents a description of the processing algorithms used to extract segment misalignment from interferograms. Some representative results of the tests carried out in the laboratory are shown in section 6. Finally, in section 7, the general conclusions are presented.

2. The UPC-ZEBRA interferometer

The UPC-ZEBRA interferometer is based on a classical Michelson interferometer layout (Twyman–Green variation). The use of an interferometric technique allows the measuring of segment misalignment during the daytime with nanometric accuracy, which was a major design guideline. A 3D layout of the interferometer is shown in figure 3.

In order to obtain the desired piston measurements, the measurement beam (MB) of the interferometer is projected onto the contact region between segments (intersegment region) in a direction locally perpendicular to them. This beam will be projected so that it evenly illuminates both segments. The reference beam (RB) of the interferometer is projected entirely onto one of the segments in a region situated as close as possible to the intersegment region of contiguous segments whose relative position has to be determined. It is also projected in the direction locally perpendicular to the segment at the projection point. This has some advantages over the classic Twyman–Green optical test set-up. Firstly, the use of an external reference mirror, which is part of one of the segments, provides a high degree of vibration insensitivity, and at the same time providing what is known as wavefront matching. This means that, even though the primary mirror is a hyperboloid, the interference pattern will look the same, regardless of which intersegment region is under analysis.

Another modification is the use of a high aperture beamsplitter cube. It is necessary to use a cube because complete geometrical symmetry between the measurement and reference arms is needed as the measuring principle is based on broadband spectrum interferometry. Another modification is the use of large diameter optics (50 mm diameter). This is necessary because a large observation area is required in order to minimize the effect of segment polishing errors on measurement accuracy, which are expected to be large near the segment edges. The last modification is the introduction of an afocal imaging system in the observation arm. This system allows imaging of the segments on the CCD array (45.3 mm $\times$ 34 mm field of view) while simultaneously reducing the size of the incoming wavefront so that it matches the CCD array size. Thus, the simultaneous observation of the interference pattern and an image of the segments allows a direct phase assignment to each point of the intersegmental region under analysis. Imaging the segments is also very useful in aligning and positioning the interferometer.

3. Description of the illumination spectrum

The measuring principle is based on a novel optical fibre illumination technique that allows the simultaneous observation of narrowband and broadband interference patterns. This technique combines light of different bandwidths (narrowband and broadband) using an optical

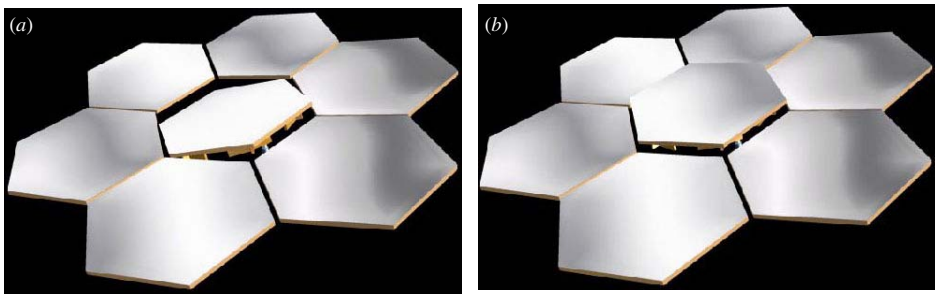

Figure 2. Segment misalignment. (*a*) Angular misalignment and (*b*) vertical misalignment.

fibre. In our set-up this is accomplished by separately filtering the light from a broadband source (halogen lamp) with two different filters (narrowband and neutral) and then coupling both to an optical fibre. The fibre spatially averages this uneven spectrum distribution in such a way that at the output a uniform spatial distribution of the light spectrum is obtained, a composite of a narrowband component over a broadband background.

This spectrum, called a *composite spectrum*, can be modelled by the addition of the models of a narrowband and a broadband spectrum, properly weighted according to the percentage of each light contained in the composite spectrum:

$$L_C(\lambda) = w_{NB} L_{NB}(\lambda) + w_{BB} L_{BB}(\lambda) \qquad (3.1)$$

where $L_C(\lambda)$, $L_{NB}(\lambda)$ and $L_{BB}(\lambda)$ are the radiances of the composite, narrowband and broadband spectra, respectively, and w_{NB} and w_{BB} are the narrowband and broadband weights, respectively.

The narrowband spectrum, obtained by filtering a broadband spectrum with an interference filter, can be modelled by a Gaussian spectrum with a given bandwidth (FWHM, $\Delta\lambda$) centred at a given wavelength (λ_0). Nominal values of the filter are $\lambda_{0NB} = 632.8$ nm and $\Delta\lambda_{NB} = 10$ nm:

$$L_{NB}(\lambda) = L_{0NB} \exp[-4 \ln 2(\lambda - \lambda_{0NB}/\Delta\lambda_{NB})^2] \qquad (3.2)$$

where L_{0NB} is the radiance when $\lambda = \lambda_{0NB}$.

The broadband spectrum is obtained when filtering the light from the halogen lamp using a neutral filter. Even though the light emitted by the lamp has a broadband spectrum, a neutral filter is needed in order to reduce the intensity of the light so that the broadband illumination level matches the narrowband illumination level. It can be inferred from the curves provided by the manufacturer that the lamp used in our set-up will behave as a grey body at 2880 K with an emissivity (ε) of 0.425. Therefore, the broadband spectrum can be modelled by a grey body spectrum, but reduced by the neutral filter by a factor independent of wavelength:

$$L_{BB}(\lambda) = L_{0BB} \frac{2c^2 h}{\lambda^5 (e^{hc/\lambda kT} - 1)} \qquad (3.3)$$

where L_{0BB} is a constant that includes the effect of the emissivity of the lamp and the transmittance of the neutral filter.

In figure 4, the experimentally measured composite spectrum and the fitted modelling equation are shown. From the fitted data, it can be inferred that the assumption that the spectra would simply add is correct. The composite spectrum is made of a broadband component that can be modelled as a grey body spectrum (2807 K) plus a narrowband component centred at 634.2 nm with a band pass of 13.2 nm. The value of the weights (w_{NB}, w_{BB}), which depend on the amount of each light contained in the composite light, are set manually.

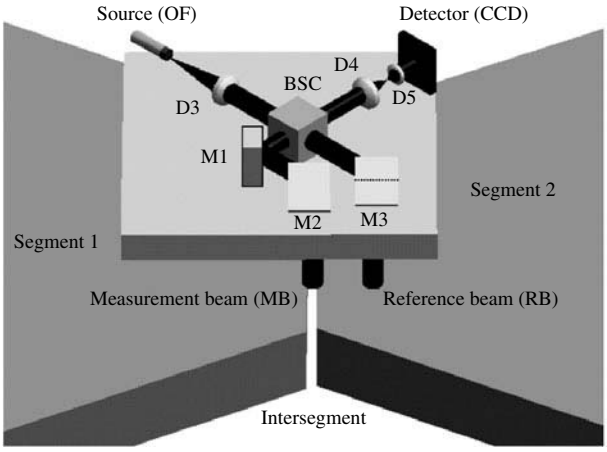

Figure 3. 3D layout of the UPC-ZEBRA interferometer.

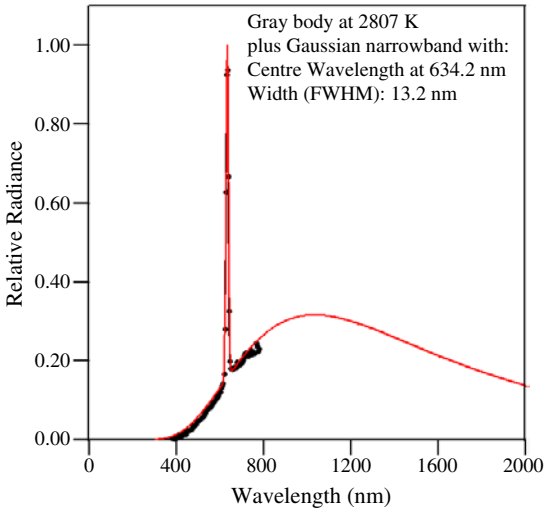

Figure 4. Measured composite spectrum and fitted modelling equation.

4. Simulation of expected interferograms

As stated in section 2, the MB is projected onto the intersegment region in a direction locally perpendicular to the segments. The RB is projected entirely onto a region of one of the segments situated as close as possible to the intersegment region, also in the direction locally perpendicular to the segment projection region.

The optical path difference (OPD) will be calculated assuming ideal wavefronts in the sense that they will be considered flat and infinite. Even though the wavefronts impinging on the segments will be flat (collimated beam) the reflected ones will no longer be flat as the segments are part of a hyperboloid. The fact of considering the reflected wavefronts to be flat will not introduce significant errors in the analysis that follows, as the effects due to segment curvature for typical values of large segmented telescopes ($\lambda/20$ astigmatism) are similar to the optical quality of the optics used in the interferometer. This is shown in Pinto (2002).

These simulations will provide an easy way to analyse the expected interferograms as a function of the different types of possible misalignments: tip, tilt and piston between segments.

In order to obtain a certain number of fringes in the interferogram, some tilt is introduced between the reference and measurement beams. This tilt also sets the desired value for the piston measurement range, which is only limited by the fringe sampling at the CCD array to a maximum of approximately 30 μm. This tilt is introduced using the angular positioner of mirror M3. In all the simulations, a typical value for the tilt between beams of 20.52 arcsec is used, and the piston measurement range for this value is set to approximately 2 μm.

The light spectrum will be the 'composite' spectrum shown in section 3. To obtain the interference pattern from the OPD calculated for each simulation condition, the expressions for partial coherence interferometry will have to be used (Goodman 1985):

$$I = I_0[1 + \mathrm{Re}\{\gamma(\tau)\}] \tag{4.1}$$

where I is the intensity that reaches the detector, I_0 is the intensity that enters the interferometer, τ is the time delay between beams and $\gamma(\tau)$ is the complex degree of coherence of the light spectrum. Re stands for the real part of $\gamma(\tau)$, as this is a complex quantity. The modulus of the complex degree of coherence of a light spectrum is a generalization of the concept of contrast (or visibility) of an interference pattern.

The complex degree of coherence is a normalized version of another quantity called the self-coherence function $\Gamma(\tau)$, which is the autocorrelation function of the optical field. A relationship between this quantity and the spectrum of the light is found using the Wiener–Khinchin theorem:

$$\Gamma(\tau) = \int_{-\infty}^{\infty} G(\nu)\exp(-\mathrm{i}2\pi\nu\tau)\,\mathrm{d}\tau \tag{4.2}$$

where $G(\nu)$ is the power spectral density of the light. This theorem states that the self-coherence function of a given optical field and its power spectral density are a pair of Fourier transforms.

The 'composite' light power spectral density can be extracted from the analysis carried out in section 3, leading to

$$\begin{aligned} G_C(\lambda) &= w_{NB}G_{NB}(\lambda) + w_{BB}G_{BB}(\lambda) \\ &= w_{NB}G_{0NB}\exp[-2\sqrt{\ln 2}(\lambda - \lambda_{0NB}/\Delta\lambda_{NB})^2] \\ &\quad + w_{BB}G_{0BB}\frac{2c^2h}{\lambda^5(\mathrm{e}^{hc/\lambda kT} - 1)}. \end{aligned} \tag{4.3}$$

In order to obtain the expected composite interferograms, the composite spectrum has to be weighted by the CCD camera responsivity before it is used to calculate the expected intensity pattern. A Gaussian response is assumed for the CCD camera (deduced from data provided by the manufacturer) with a maximum at 520 nm with a FWHM of 400 nm. This curve has to be truncated at 400 nm to include the effects of optics cutoff.

The expected interferograms for four misalignment conditions, (*a*) no misalignment, (*b*) $\lambda/2$ piston, (*c*) tilt and (*d*) tip are shown in figure 5. An equal weight for the narrowband and the broadband components (0.5) has been used. It has also been assumed that there is no tip between the reference and measurement wavefronts. Note that, due to the orientation of the CCD camera, the intersegment is imaged in the horizontal direction.

The interferograms show three clearly separated regions (see figure 5): (i) the upper sub-field, where the reference wavefront (from segment 2) interferes with the half of the measuring wavefront that comes from segment 1, (ii) the intersegment area and (iii) the lower sub-field, where the reference wavefront interferes with the half of the measuring wavefront that comes from the same segment (segment 2).

When 'composite' light is used in an interferometer, the fringe pattern obtained is the sum of a narrowband and a broadband fringe pattern. If the balancing is done properly, both types of interferograms can be observed at the same time. Therefore, what is obtained is basically a monochromatic interference pattern (due to the narrowband part of the spectrum) with a pair of fringes, those closer to an OPD of zero (due to the broadband background) having a maximum intensity greater than the rest. In this way, an absolute reference has been introduced into a monochromatic interference pattern, thus allowing us to unambiguously remove the $\lambda/2$ indetermination.

From simulated interferograms one can infer that the presence of piston will lead to fringe mismatching in the interference pattern. Residual tip and tilt angular misalignment will also have an effect on the upper sub-field fringe pattern, allowing them also to be extracted: relative tilt between segments will cause the fringe period to change, and relative tip will cause the fringes to deviate from the vertical in the upper sub-field.

5. Segment misalignment extraction algorithms

The main objective of the processing algorithms is to allow the measurement of segment misalignment from a single interferogram.

These interferograms have been specifically developed to measure piston between segments. It is clear from figures 2(*a*) and (*b*) that piston is not well defined if there is tilt and/or tip between segments. The piston measurement procedure has to be carried out after tip and tilt between segments have been

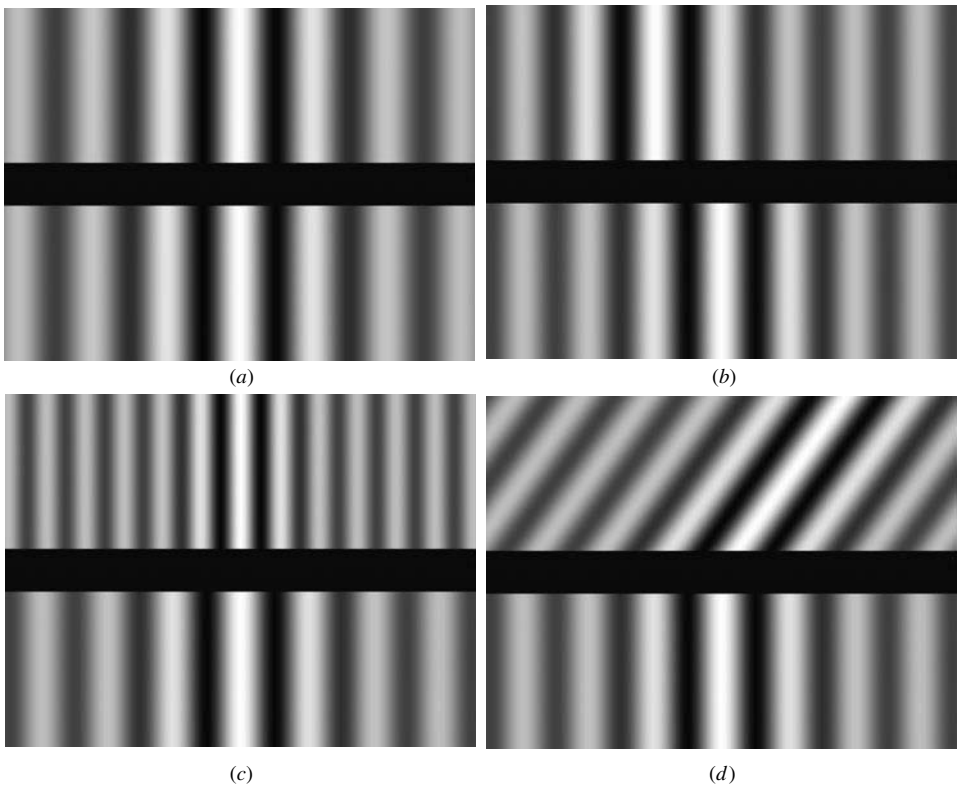

Figure 5. Expected interferograms for some misalignment conditions: (*a*) no misalignment, (*b*) piston, (*c*) tilt and (*d*) tip.

removed. This is usually done using a tip/tilt wavefront sensor such as a Shack–Hartmann camera. However, interferograms are also processed to extract tip/tilt between wavefronts and between segments as a way to check that the alignment conditions for proper piston extraction were satisfied. In this way, residual tip and tilt between segments can also be measured, and a better alignment than that obtained using the tip/tilt wavefront sensor alone can be achieved.

Another alignment condition that has to be satisfied for proper piston extraction is the absence of tip between the reference and measurement wavefronts. This can easily be achieved using the internal mirror positioners of the interferometer. Yet another alignment condition is that the OPD between the measurement and reference beam paths be close to zero; otherwise the interference pattern due to the broadband component would not be observed within the field of view of the CCD camera.

The algorithms can be divided into two sub-categories: data extraction algorithms and data processing algorithms. The former are used to extract data from interferograms and the latter are used to calculate piston error from the extracted data.

The data extraction procedure will begin by selecting the rows of the digitized interferogram that will be used as data input. One could use the whole interferogram, but a few lines evenly spread over each sub-field will be enough to provide reliable data while reducing the computation time.

5.1. Data extraction algorithms

Data will be extracted using two procedures: a fit of experimental data to the theoretical monochromatic intensity pattern which will provide information on typical monochromatic parameters such as fringe period and initial phase, and a maximum intensity search procedure that will provide the reference for the zero OPD typical of white-light interferometry.

The theoretical expression that will be fitted to each line of experimental data can be expressed as

$$I^j(i) = I_1^j + I_2^j \cos\left[\frac{2\pi}{T_j}\mathrm{i} + \varphi_0^j\right] \qquad \text{(8-bit grey value)} \quad (5.1)$$

where $I^j(i)$ is the intensity of the ith pixel of the jth row, I_1^j is the mean intensity, I_2^j is the difference between the maximum or minimum value and mean value (related to interferogram contrast), T_j is the period in pixels and φ_0^j is the initial phase.

The method used to fit the data is the Levenberg–Marquard non-linear least-squares fit (Press *et al* 1996). Once this procedure has been executed the fringe period and initial phase for each selected row are obtained.

The next step in the data extraction procedure is the location of the maximum intensity pixel for each row. A simple maximum value search algorithm is implemented:

$$X_M^j = \max[I^j(i)] \qquad \text{(pixels)}. \quad (5.2)$$

Another parameter that will be used in the data processing algorithms will be the number of lines used in each sub-field. We will refer to it as L_{USED}, and it is assumed that the same number of lines will be used in each sub-field and that they will be evenly distributed.

5.2. Data processing algorithms

These algorithms will use the data extracted from the interferograms to calculate the values of segment misalignment (tip, tilt and piston), as well as other data such as tip and tilt between the reference and measurement wavefronts.

Certain parameters related to the characteristics of the CCD camera and to the field of view will also be needed in the data processing algorithms:

- The number of pixels of the CCD array in the X direction, $\boldsymbol{N}$.
- The field of view in the X direction (in mm), $\boldsymbol{\Delta x}$.
- The segment sampling size in the X direction, $\mathrm{d}\boldsymbol{x} = \boldsymbol{\Delta x}/\boldsymbol{N}$.

5.2.1. Average fringe period ($\bar{T}$). The average fringe period will be calculated as the average of the fringe periods for all the selected lines in each sub-field:

$$\bar{T} = \mathrm{avg}(T_j) = \sum_j T_j / L_{USED} \qquad \text{(pixels)}. \tag{5.3}$$

5.2.2. Average maximum intensity position ($\bar{X}_M$). The first step of this algorithm will consist in calculating the average value of the position of maximum intensity for each sub-field. This value will be calculated as:

$$\bar{X}_M = \mathrm{avg}(X_M^j) = \sum_j X_M^j / L_{USED} \qquad \text{(pixels)}. \tag{5.4}$$

The second step will refine the average maximum intensity position. Using the initial phase (φ_0^j) from the monochromatic fit, this position can be recalculated with sub-pixel accuracy.

5.2.3. Piston measurement range (M_R). From the basic equation that defines the interferograms, one can infer that one fringe period, in pixels, corresponds to $\lambda/2$ piston, in nanometres (or OPD of λ, as the OPD is doubled because of reflection). Therefore, the piston measurement range, which is the difference between the maximum and minimum piston values that can be measured, will be $\lambda/2$ times the number of fringes in the interferogram of the upper sub-field ($N/\bar{T}_{UPPER}$):

$$M_R = \frac{\lambda}{2}\frac{N}{\bar{T}} \qquad \text{(nm)}. \tag{5.5}$$

If piston error is within this range it will be measured properly, as the maximum intensity fringe (which is the reference for zero OPD) will be within the field of view. This value is set using one of the internal mirror positioners of the interferometer.

5.2.4. Calibration factor (C_F). This is the value used to convert lateral pixel displacement into nanometres in the vertical direction on the segments. It is measured in nanometres per pixel (nm/pixel). One can say that it is the measurement range for each pixel:

$$C_F = \frac{M_R}{N} = \frac{\lambda}{2\bar{T}_{UPPER}} \qquad \text{(nm/pixel)}. \tag{5.6}$$

5.2.5. Piston error (P). In order to determine the piston error, a simple calculation must be made. The average maximum intensity position (corresponding to zero OPD) has been calculated for each sub-field (see expression (5.4)). As the conversion factor between pixels and nanometres has also been calculated (expression (5.6)), the piston error can be found from

$$P = C_F(\bar{X}_M^{UPPER} - \bar{X}_M^{LOWER}) \qquad \text{(nm)}. \tag{5.7}$$

5.2.6. Tilt between segments (θy_{MR}). As shown in the interferogram simulation section, the presence of tilt between segments leads to a change in the upper sub-field fringe period with regard to the fringe period in the lower sub-field, which is only related to the tilt between the measurement and reference wavefronts.

Because of the design of the interferometer, tilt between segments (θy_{12}) can be calculated from

$$\theta y_{12} = \frac{1}{2}\left[\tan^{-1}\left(\frac{\lambda}{\bar{T}_{UPPER}\,\mathrm{d}x}\right) - \tan^{-1}\left(\frac{\lambda}{\bar{T}_{LOWER}\,\mathrm{d}x}\right)\right] \qquad \text{(arcsec)}. \tag{5.8}$$

5.2.7. Tip between segments ($\theta \boldsymbol{x}_{12}$). As has also been seen in the section on interferogram simulation, the presence of tip between segments leads to a change in the fringe inclination in the upper sub-field, related to segment 1, with regard to the fringe inclination in the lower sub-field, related only to the tip between the measurement and reference wavefronts. The tip between wavefronts is set as close as possible to zero using the internal mirror positioners of the interferometer.

The tip between segments can be expressed as

$$\theta x_{12} = \frac{1}{2}\left[\tan^{-1}\left[\left(\frac{\Delta\varphi_0}{\Delta j}\right)_{UPPER}\frac{\lambda}{2\pi}\frac{1}{\mathrm{d}x}\right] - \tan^{-1}\left[\left(\frac{\Delta\varphi_0}{\Delta j}\right)_{LOWER}\frac{\lambda}{2\pi}\frac{1}{\mathrm{d}x}\right]\right] \qquad \text{(arcsec)} \tag{5.9}$$

where $(\Delta\varphi_0/\Delta j)$ is the gradient of the initial phase in the given sub-field.

Under real conditions these algorithms should be slightly modified to include the effects of segment figure errors. Accurate maps of the individual segments will be provided by the manufacturer.

6. Results

Intensive tests were conducted in our laboratory. A two-segment simulation system was built for preliminary tests in a controlled environment, before carrying out the experiment at the GTC test bench. This two-segment simulation system includes tip, tilt and piston displacement capability plus an independent relative displacement sensor by Hewlett–Packard (HP10719A) that is used as a reference. The following plots show accuracy and repeatability tests conducted in our laboratory.

In figure 6, a time series of piston has been plotted. In this case the measurement region was a single mirror. Therefore this is a measurement of what we call zero-piston.

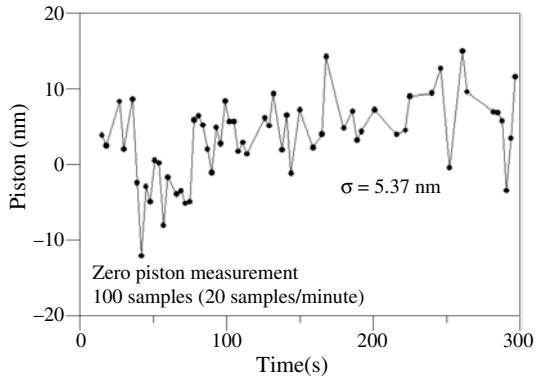

Figure 6. Zero-piston test.

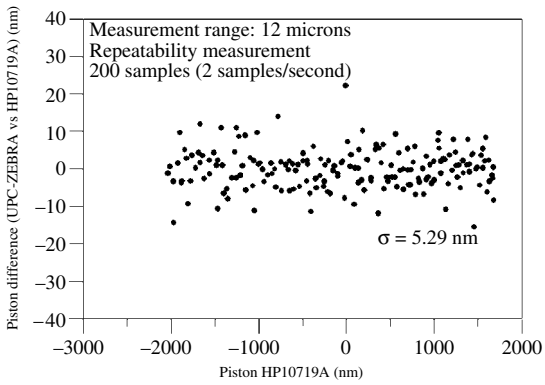

Figure 7. Repeatability test.

For repeatability measurements the piston was usually ramped from -2 to $+2$ μm while measurements were being taken. Figure 7 plots the difference between the piston measured by our instrument and the piston measured by the reference system as a function of the value of the piston provided by the reference instrument.

A paper on instrument testing is now in preparation. It will include both a detailed description of the tests carried out and the most relevant results obtained.

7. Conclusions

A novel illumination technique which allows simultaneous observation of a narrowband and a broadband interference pattern has been presented. This technique allows an absolute reference to a monochromatic interferogram to be introduced, thus removing the $\lambda/2$ indetermination. A modelling of such an illumination spectrum ('composite' spectrum) has been presented. The experimentally measured spectrum shows perfect agreement with the modelled spectrum.

A simulation of expected interferograms using such a spectrum has been presented. This simulation has shown that piston error as well as tip and tilt between segments can be measured simultaneously using only a single interferogram. The algorithms used to extract segment misalignment from interferograms are also presented in detail.

From the tests that have been carried out, one can conclude that the interferometer is able to measure piston between segments with a repeatability of 5 nm (1σ) in a piston range of 30 μm.

Acknowledgments

The authors would like to thank J Arasa, C Pizarro and N Tomàs, who contributed substantially to the design of the instrument. The authors also wish to thank Grantecan S A and CICYT for the funds provided for the development of this project. AP would like to thank the Department of Universities, Research and the Information Society for the PhD grant he received, which enabled him to take part in this work.

References

Chanan G, Troy M, Dekens F, Michaels S, Nelson J, Mast T and Kirkman D 1998 Phasing the mirror segments of the Keck telescopes: the broadband phasing algorithm *Appl. Opt.* **37** 140–55

Goodman J W 1985 *Statistical Optics* (New York: Wiley)

Grantecan S A 1997 *GTC Conceptual Design* (La Laguna, Tenerife: GTC Project Office)

Pintó A 2002 New interferometric technique for piston measurement and phasing of segmented mirrors *PhD Thesis* Optics and Optometry Department, Universitat Politècnica de Catalunya

Pizarro C, Arasa J, Laguarta F, Tomàs N and Pintó A 2002 Design of an interferometric system for the measurement of phasing errors in segmented mirrors *Appl. Opt.* **41** 4562–70, and references cited therein

Press W H, Teukolsky S A, Vettering W T and Flannery B P 1996 *Numerical Recipes in C. The Art of Scientific Computing* 2nd edn (New York: Cambridge University Press) p 656